Nanoscale

PAPER

View Article Online
View Journal

Cite this: DOI: 10.1039/d5nr05061h

Design of a 2D/1D $Bi_2MoO_6/Bi_{19}S_{27}Br_3$ direct Z-scheme heterojunction with a built-in internal electric field for enhanced photocatalytic CO_2 reduction performance

Zakaria Ismail, [a] You Li,[a] Jian Lei,[b] Saira Man,[a] Khadija Tul Kubra,[c] Chao Zhang, *[b] Jingxiang Low [d] and Yujie Xiong *[a,b]

Bi-based heterojunctions have garnered extensive attention for photocatalytic carbon dioxide (CO_2) reduction due to their efficient charge separation and strong redox ability. The built-in internal electric field (IEF) at the interface of a direct Z-scheme heterojunction interface serves as the driving force for charge transfer; however, suboptimal interfacial contact often restricts carrier migration efficiency. Herein, we meticulously tune the contact interface over a Bi-based heterojunction by modulating the morphologies of the semiconductor components. Specifically, we synthesize a 2D/1D Bi_2MoO_6/$Bi_{19}S_{27}Br_3$ (BMO/BSBr) direct Z-scheme heterostructure by embedding 1D BSBr nanorods onto 2D BMO nanosheets. Such a contact interface can optimize photogenerated charge carrier migration between BMO and BSBr, thereby significantly promoting their separation. As a result, the photocatalytic CO_2 conversion performance of the optimized BMO/BSBr reaches 34.4 μmol g^{-1} h^{-1}, exceeding those of BMO and BSBr by 4.5- and 19.8-fold, respectively. The mechanisms underlying this enhanced photocatalytic performance are revealed *via in situ* diffuse reflectance infrared Fourier transform spectroscopy (DRIFTS), X-ray photoelectron spectroscopy and radical trapping tests, showing that the internal electric field along with the fine-tuned contact interface holds the key to significantly boosting photogenerated charge carrier utilization efficiency. This study provides a novel design strategy for constructing high-performance photocatalysts *via* interfacial chemical bonding, offering efficient charge transfer and high catalytic activity.

Received 1st December 2025,
Accepted 27th February 2026

DOI: 10.1039/d5nr05061h

rsc.li/nanoscale

Introduction

The evolution of photocatalysis, which relies solely on incident solar energy for driving chemical reactions, provides a potential solution for resolving energy crises and environmental issues.[1–4] Amidst the development of photocatalysis, photocatalytic CO_2 conversion has attracted widespread attention, as it can simultaneously mitigate CO_2 concentration in the atmosphere and produce valuable chemicals.[5–7] Throughout recent decades, vast arrays of photocatalytic semiconductor materials have been engineered for use in photocatalytic CO_2 reduction.[7–12] However, due to intense electron–hole pair recombination, insufficient catalytically active centers, and the high bond energy barrier for dissociation of the C=O bond (750 kJ mol^{-1}), achieving efficient photocatalytic CO_2 reduction remains challenging in practical production.[13,14] Therefore, the current efficiency of photocatalytic CO_2 reduction falls far below the threshold required for industrial standards.[15–17]

Focusing on optimizing the three critical steps in the photocatalytic CO_2 reduction process, a central challenge lies in engineering photocatalytic materials with superior light harvesting, sufficient catalytically active centers, and highly efficient electron–hole pair separation. Countless strategies have been pursued to address these limitations, such as vacancy engineering,[18–20] constructing ultra-thin structures,[21,22] doping elements,[23,24] and fabricating heterojunctions.[25,26] The construction of heterojunctions has

[a]School of Chemistry and Materials Science, Hefei National Research Center for Physical Sciences at the Microscale, Key Laboratory of Precision and Intelligent Chemistry, University of Science and Technology of China, Hefei, Anhui 230026, China. E-mail: yjxiong@ustc.edu.cn
[b]Anhui Engineering Research Center of Carbon Neutrality, The Key Laboratory of Functional Molecular Solids, Ministry of Education, Anhui Laboratory of Molecular-Based Materials, College of Chemistry and Materials Science, Anhui Normal University, Wuhu, Anhui 241002, China. E-mail: zc1992@ustc.edu.cn
[c]National Synchrotron Radiation Laboratory, School of Nuclear Science and Technology, The Experimental Center of Engineering and Material Sciences, University of Science and Technology of China, Hefei, Anhui 230026, China
[d]School of Physical Science and Technology, School of Materials Science and Engineering, Tiangong University, Tianjin 300387, China

been extensively studied in photocatalytic CO_2 reduction.[27–29] The choice of suitable semiconductors for integrating specific heterojunction types, such as step-scheme (S-scheme)[30–32] and direct Z-scheme[33–36] configurations, is critical. The formation of strong bonds at the hetero-interface plays a crucial role in enhancing interfacial carrier migration and optimizing performance. Consequently, creating interfacial interatomic bonds in heterostructures is considered a key strategy to maximize the efficiency of photocatalytic CO_2 reduction.[37–43]

The interfacial interatomic bonds can dictate the interfacial charge distribution and minimize the interfacial resistance in the contact region, which will substantially improve the transmission and separation efficiency of photogenerated charges and enhance photoinduced catalytic activity.[44–47] A diverse range of semiconductor materials has been designed for use in photocatalytic CO_2 reduction applications. Among them, bismuth-based (Bi-based) photocatalytic materials, such as Bi_2MoO_6 (BMO),[48–50] $BiVO_4$,[51–53] and Bi_2WO_6,[54–56] have recently attracted extensive attention due to their controllable synthesis, unique crystal structures, and eco-friendliness.

BMO, as a conventional Bi-based semiconductor oxide, is regarded as a promising photocatalytic material as a result of its durable, stable physicochemical properties and appropriate wide band gap (~2.7 eV).[57–59] However, there are some setbacks to the improvement of pure BMO as a photocatalyst due to its excessive electron–hole recombination rate.[60–62] Various procedures, including controlling the morphology and integrating two-dimensional (2D) BMO nanosheets (NSs) with other materials to construct a remarkable heterojunction, have been implemented to enhance charge separation efficiency and improve CO_2 adsorption capacity for CO_2 photoreduction.[62,63]

Additionally, among the Bi-based V–VI–VII group narrow bandgap semiconductors, $Bi_{19}S_{27}Br_3$ (BSBr) stands out due to its superior light absorption capability, remarkable electrical conductivity, and an appropriately positioned negative conduction band (CB) potential. These characteristics make BSBr a promising candidate for photocatalytic CO_2 reduction applications.[64–68] One-dimensional (1D) BSBr nanorods (NRs) have been extensively combined with diverse materials, such as In_2O_3, g-C_3N_4, and $SnIn_4S_8$, to build heterostructure composites with interfacial bonds, promoting the photoreduction of CO_2 to value-added products.[69–71] Based on these observations, the tight interatomic contact in the interfacial region of the heterojunction cannot be overlooked. Thus, the synergistic coupling effects between 2D/1D components together with the formation of interatomic bonds in the interfacial region of heterostructures can facilitate photoinduced charge separation and surface redox reactions to enhance the photocatalytic activity and reaction selectivity of CO_2 photoreduction.

Here, the strategic construction of a 2D/1D BMO/BSBr direct Z-scheme composite heterojunction structure, formed from 2D BMO nanosheets and 1D BSBr nanowires with a built-in internal electric field (IEF) and interfacial interatomic bonds, is anticipated to be an ideal design for achieving highly efficient photocatalytic CO_2 reduction. The presence of the IEF facilitates the combination of CB electrons from BMO and valence band (VB) holes from BSBr. Additionally, the strong built-in IEF and interatomic bond interactions prevent the dissociation of the BMO and BSBr heterojunction during the photocatalytic CO_2 reduction process, providing a relatively efficient and stable photocatalytic system. Meanwhile, electrons with high reduction ability from BSBr and holes with high oxidation ability from BMO participate in redox reactions. This study introduces an innovative approach to synergistically regulate 2D/1D direct Z-scheme heterojunction systems through a built-in IEF and interfacial interatomic bonding to achieve efficient photocatalytic CO_2 reduction.

Experimental

Materials

Ammonium molybdate tetrahydrate ($(NH_4)_6Mo_7O_{24}\cdot4H_2O$), thiourea, bismuth nitrate pentahydrate ($Bi(NO)_3\cdot5H_2O$), ammonia solution, Nafion, ethylene glycol, ethanol and cetyltrimethylammonium bromide (CTAB) were purchased from Shanghai Sinopharm Chemical Reagent Co. Ltd (P. R. China). Deionized (DI) water was used throughout the study. All reactants were of analytical purity and used as received, without further purification.

Preparation of BMO

In a typical synthesis, BMO was prepared *via* a hydrothermal method. First, 3 mmol of $Bi(NO)_3\cdot5H_2O$ was dispersed in 40 mL of DI water under magnetic stirring for 30 min to ensure complete dissolution. Subsequently, 0.214 mmol $(NH_4)_6Mo_7O_{24}\cdot4H_2O$ was added to the solution under continuous stirring for an additional 30 min to form a homogeneous precursor mixture. The pH of the solution was then adjusted to neutral (pH = 7) by dropwise addition of ammonium hydroxide (NH_4OH, 28%) under constant stirring. The solution was transferred into a 50 mL Teflon-lined autoclave for thermal treatment at 160 °C for 10 h. The sample was collected by centrifugation and washed several times using DI water. The final product was dried in a vacuum oven at 70 °C for 24 h obtain BMO NSs.

Preparation of *X*-BMO/BSBr and BSBr

The *X*-BMO/BSBr composites (where *X* = 1, 2, 3 and 4 correspond to 10, 20, 40, and 80 mg of BMO, respectively) were synthesized through a modified solvothermal method. In a typical procedure, the predetermined amount of BMO was first dispersed in 30 mL ethylene glycol under vigorous magnetic stirring for 30 min. Subsequently, 0.46 mmol thiourea, 0.40 mmol CTAB, and 0.02 mmol $Bi(NO)_3\cdot5H_2O$ were sequentially added to the suspension. The mixture was maintained under continuous vigorous stirring for 4 h at room temperature to ensure complete precursor homogenization. The solution was then transferred to a 50 mL Teflon-lined autoclave and subjected to thermal treatment at 403 K for 10 h. Subsequently, the products were collected by centrifugation and washed

alternately with ethanol and DI water many times. Then, the samples were dried in a vacuum oven at 343 K for 24 h. For comparison, pristine BSBr was synthesized following an identical method without the addition of the BMO precursor.

Results and discussion

Characterization and preparation of catalysts

In this work, 2D/1D BMO/BSBr heterostructure composites were synthesized by mixing the primary precursors under controlled conditions using the solvothermal method, and the construction process is depicted in Fig. 1a. The interfacial interactions between 1D BSBr NRs and 2D BMO NSs in the BMO/BSBr heterostructure were further investigated. The X-ray diffraction (XRD) patterns of pure BMO, BSBr, and the synthesized BMO/BSBr composites are demonstrated in Fig. 1b. The diffraction peaks of the synthesized BMO at 2θ values of 28.3°, 32.5°, 33.1°, *etc.*, can be assigned to the crystal planes (131), (200), (060), *etc.*, respectively, matching with the orthorhombic crystal structure of BMO (JCPDS Card no. 21-0102).[72] Moreover, the prepared BSBr demonstrates XRD peaks attributed to hexagonal BSBr (JCPDS Card no. 26-0813).[68] In addition, all the synthesized BMO/BSBr heterostructures demonstrate XRD peaks attributed to BMO and BSBr. However, as the concentration of BMO increased, the diffraction peak corresponding to the (131) crystallographic plane of BMO exhibited a significant increase in sharpness (Fig. 1c), suggesting successful coupling of these two semiconductors.

Fourier transform infrared (FTIR) spectra (Fig. 1d) of BMO, BSBr, and BMO/BSBr were also obtained to shed some light on their surface functional groups. The primary absorption bands of BMO, observed in the range of 400–950 cm^{-1}, are associated with the stretching vibrations of Bi–O and Mo–O bonds, as well as Mo–O–Mo bridging stretching modes.[73,74] Additionally, the peaks at 1380 cm^{-1} are attributed to the O–H stretching vibration of the surface adsorbed H_2O.[75] Moreover, the BSBr spectrum showed a weak peak at 500 cm^{-1}, belonging to the vibrational state of the Bi–O bonds.[49,70,76] Notably, after coupling BMO with BSBr, the FTIR spectrum of BMO/BSBr exhibits negligible changes, suggesting that the presence of BSBr does not alter the surface functional groups on BMO.

X-ray photoelectron spectroscopy (XPS) was assessed for gaining insights into the compositional structures and surface elemental and chemical valence of the prepared samples. The high-resolution Bi 4f, S 2p, Mo 3d, Br 3d, and O 1s XPS spectra of BMO, BSBr, and 2-BMO/BSBr are shown in Fig. 2. As shown in Fig. S1, Bi, Mo, S, Br, and O elements can be observed in the XPS survey spectrum of the 2-BMO/BSBr composite, confirming coupling of BMO with BSBr. In the high-resolution Bi 4f and S 2p XPS spectra (Fig. 2a), the deconvoluted peaks of the BMO and BSBr samples reveal two distinct binding energy peaks corresponding to the Bi-4$f_{5/2}$ and Bi-4$f_{7/2}$ doublet, confirming the presence of Bi^{3+} in both materials. In the 2-BMO/BSBr heterojunction, the observed signals of Bi 4f can be assigned to Bi^{3+} ions, originating from both the BMO[77–79] and BSBr[72,80,81] components. Furthermore, all Bi 4f peaks in the heterojunction exhibit a clear shift toward lower binding energy compared to the individual components, a direct result

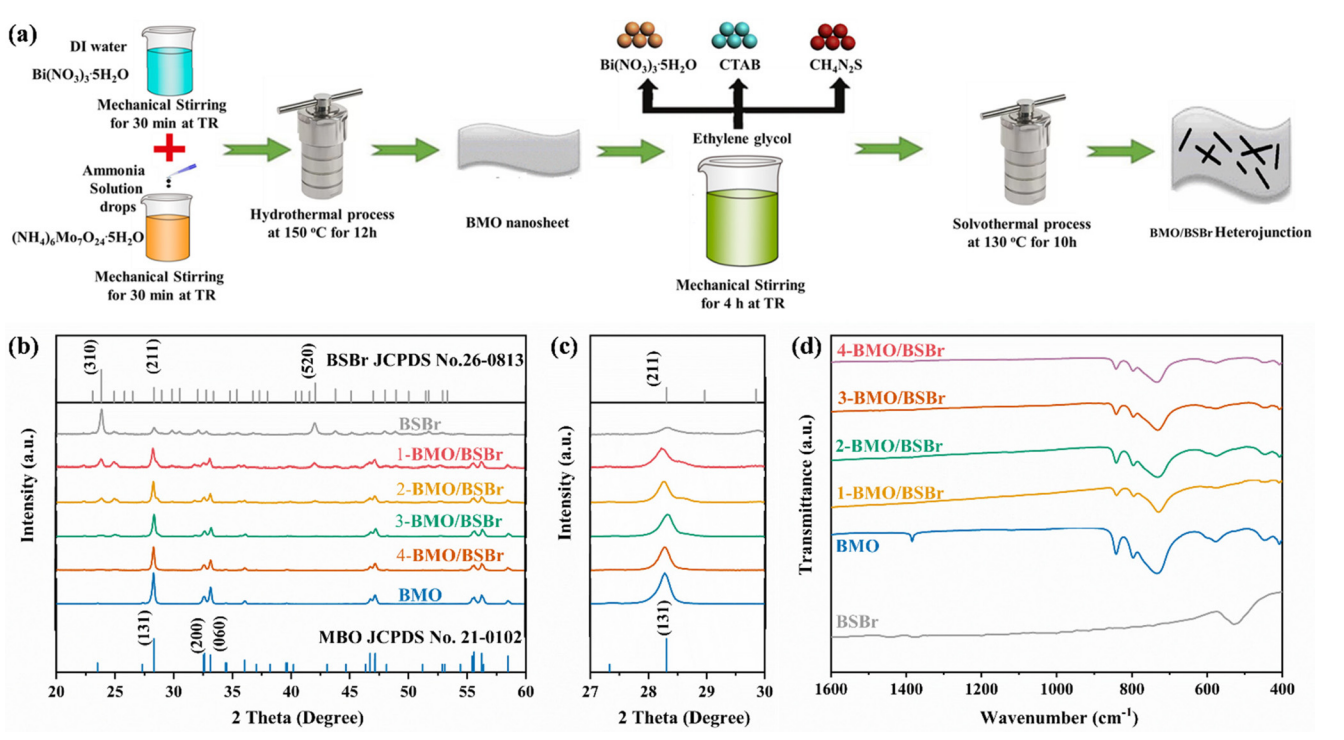

Fig. 1 (a) Preparation process of BMO/BSBr heterojunctions. (b and c) XRD patterns and (d) FTIR spectra of BMO/BSBr heterojunctions.

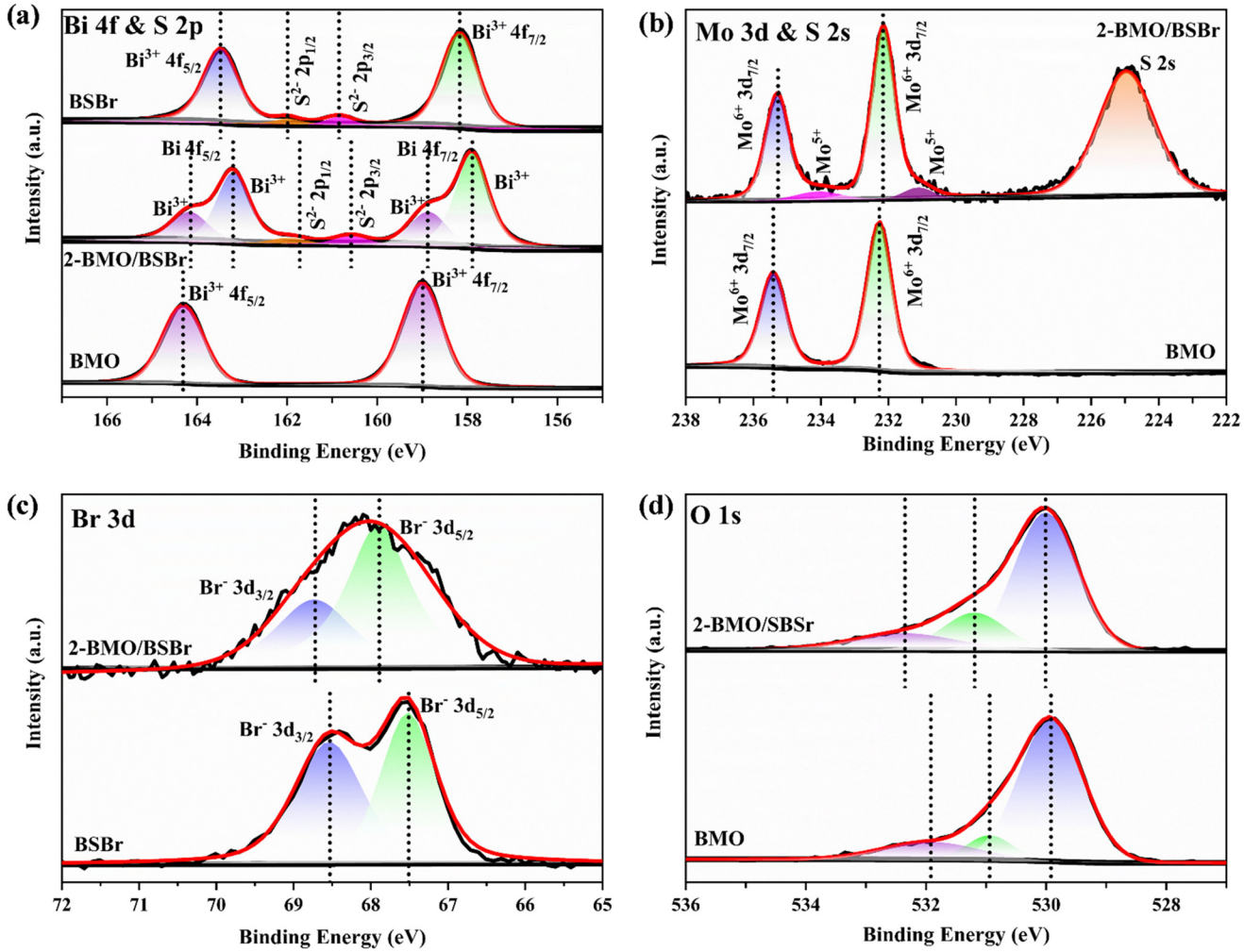

Fig. 2 (a–d) XPS spectra of Bi, S, Mo, Br, and O in BMO, BSBr, and 2-BMO/BSBr.

of electronic interactions at the heterojunction interface. Meanwhile, the deconvoluted peaks of S 2p for both bare semiconductors and the 2-BMO/BSBr composite (Fig. 2a) correspond to S-2$p_{1/2}$ and S-2$p_{3/2}$ states, confirming the presence of S^{2-} in all materials.[82] As a result of heterojunction formation, these two S 2p peaks shift to a lower binding energy. In Fig. 2b, the BMO sample reveals two distinct strong binding energy peaks corresponding to Mo 3$d_{7/2}$ and Mo 3$d_{5/2}$, respectively. For the 2-BMO/BSBr sample, these peaks are still present but shift slightly to a lower binding energy, confirming the presence of Mo^{6+} in both materials. Additionally, a new peak at 224.98 eV appears in the composite, indicating the formation of a Bi–S bond at the BMO and BSBr heterojunction interface.[72,76] Furthermore, two weak peaks located at 234.04 and 231.07 eV indicate the presence of Mo^{5+}.[83] In Fig. 2c, BSBr and 2-BMO/BSBr spectra reveal two deconvoluted peaks corresponding to Br 3$d_{3/2}$ and Br 3$d_{5/2}$, confirming the presence of Br^- in the samples.[84,85] In the 2-BMO/BSBr heterojunction, these peaks shift to a higher binding energy compared to bare BSBr. The deconvoluted O 1s XPS spectra of BMO (Fig. 2d) exhibit three distinct peaks, which can be assigned to Mo–O, Bi–O, and surface adsorption oxygen, respectively.[86,87] The same peaks are also observed in the 2-BMO/BSBr heterojunction, but with a shift to higher binding energy. This shift confirms the loading of BMO on BSBr. Notably, the XPS results reveal a negative shift in the Bi 4f and S 2s peaks, while the Br 3d and O 1s peaks exhibited a positive shift over 2-BMO/BSBr compared to its single component counterparts,[85] suggesting charge density redistribution and confirming the presence of strong interatomic chemical bond interactions.[88]

The scanning electron microscope (SEM) image of BMO (Fig. S2a) reveals its nanosheet morphology, whereas BSBr exhibits a nanorod morphology (Fig. S2b). Fig. S2c–f further illustrate the morphological details of BMO/BSBr, confirming the effective formation of the heterojunction configuration. Transmission electron microscopy (TEM) images (Fig. S3a–c) corroborate these structural features. In addition, energy dispersive spectroscopy (EDS) elemental mapping images confirm the presence of Bi, Mo, and O in BMO and Bi, S, and Br in BSBr NRs (Fig. S3d–k). The micro-morphology of the syn-

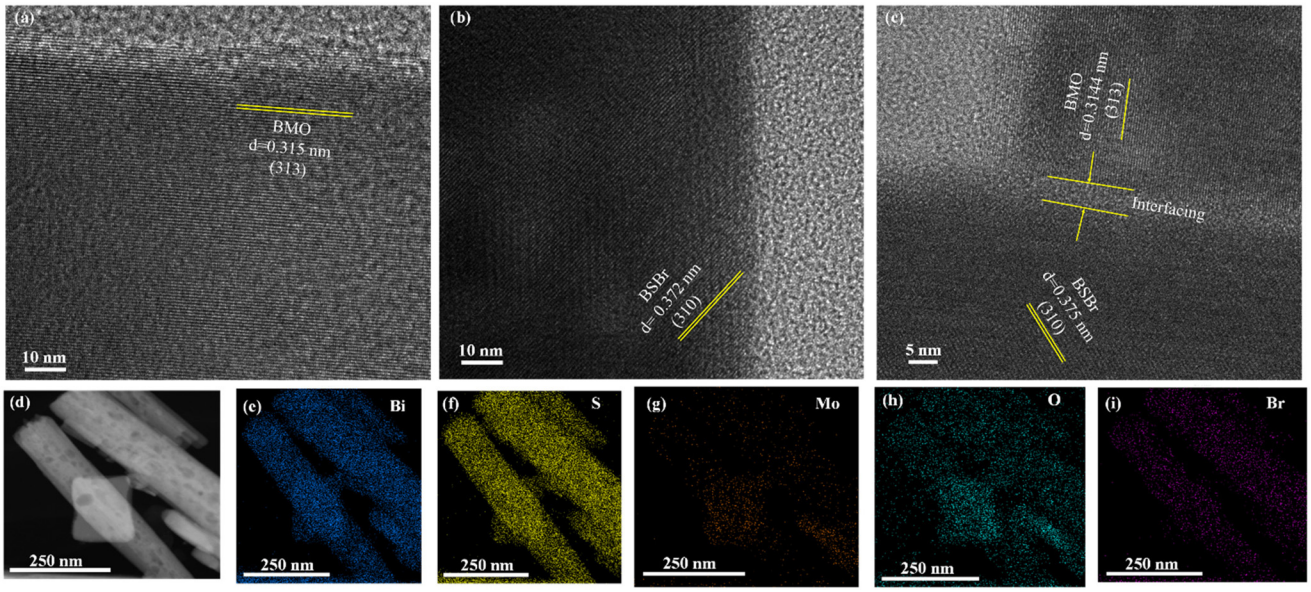

Fig. 3 (a–c) HRTEM images of BMO, BSBr, and 2-BMO/BSBr. (d–i) Elemental maps of 2-BMO/BSBr sample.

thesized samples was investigated using high-resolution TEM (HRTEM). As shown in Fig. 3a–c, lattice fringes of 0.315 and 0.372 nm can be observed on BMO and BSBr, corresponding to the (313) plane of BMO and the (310) plane of BSBr, respectively (see also Fig. S4a and b for the corresponding SAED patterns). For the 2-BMO/BSBr composite (Fig. 3c), two distinct lattice spacings of 0.314 and 0.375 nm can be identified, matching the (313) plane of BMO NSs and the (310) plane of BSBr NRs, respectively. These findings confirm the strong interfacial interaction between BSBr NRs and the surface of BMO NSs, facilitating the formation of a 2D/1D heterojunction through the synthesized process. The corresponding SAED patterns for the 2-BMO/BSBr composite are illustrated in Fig. S4c. EDS elemental maps (Fig. 3d–i) confirmed the presence of Bi, Mo, O, S, and Br within the composite materials. Additionally, EDS analysis (Fig. S5) reveals the elemental composition in the prepared 2-BMO/BSBr sample, which is consistent with the expected stoichiometric composition.

Band structures and surface structures

The optical properties of the synthesized photocatalysts were further investigated using ultraviolet-visible diffuse reflectance spectroscopy (UV-Vis DRS) (Fig. 4a). BMO displays a narrow visible light absorption edge at approximately 430 nm, while unmodified BSBr exhibits a broader absorption range and a stronger visible light absorption capacity. Significantly, the BMO/BSBr composites demonstrate a pronounced red shift in the absorption edge with increasing BSBr content compared to pure BMO, indicating enhanced visible light absorption. These results highlight the importance of optimizing both the doping ratio and heterostructure design to improve visible light harvesting and consequently enhance photocatalytic performance. Additionally, the Tauc plots, illustrated in Fig. 4b, based on UV-Vis DRS results, show that the bandgap values of BMO and BSBr are 2.75 and 1.53 eV, respectively.

To further explore the band structure of BMO and BSBr, the VB positions of the semiconductors were measured using VB-XPS. Fig. 4c depicts the VB-XPS spectra of BMO and BSBr, revealing values of 2.31 and 0.64 eV, respectively. The VB-XPS potential was calculated based on the following equation:[65]

$$E_{\text{VB-NHE}} = \varphi + E_{\text{VB-XPS}} - 4.44$$

where $E_{\text{VB-NHE}}$ is the VB potential *vs.* NHE and φ = 4.2 eV is the work function. Therefore, the $E_{\text{VB-NHE}}$ of BMO and BSBr can be determined to be 2.07 and 0.4 V, respectively. Based on these results, the band structures of BMO and BSBr can be illustrated in Fig. 4d. Specifically, the CB and VB band positions of BMO are more positive than those of BSBr, laying a foundation for the formation of the heterojunction structure and the charge flow pathway.

The surface texture is a critical factor influencing the performance of photocatalytic CO_2 reduction, as it directly determines the CO_2 adsorption capacity of the material. As shown in Fig. S6, the surface area and pore structure of BMO, BSBr, and 2-BMO/BSBr were examined using N_2 adsorption–desorption isotherms *via* the Brunauer–Emmett–Teller (BET) method. All samples exhibited type-IV adsorption–desorption curves with H3-type hysteresis isotherm loops, confirming the presence of a mesoporous structure in the synthesized materials. Furthermore, the BET surface areas of BMO and BSBr were found to be 19.23 $m^2\ g^{-1}$ and 7.11 $m^2\ g^{-1}$, respectively. After hybridization, the BET surface area of the 2-BMO/BSBr composite increased significantly to 38.32 $m^2\ g^{-1}$. This substantial increase in specific surface area for the 2-BMO/BSBr composite confirms the formation of an ideal architecture structure, which reduces the aggregation of 2D BMO NSs and 1D-shaped

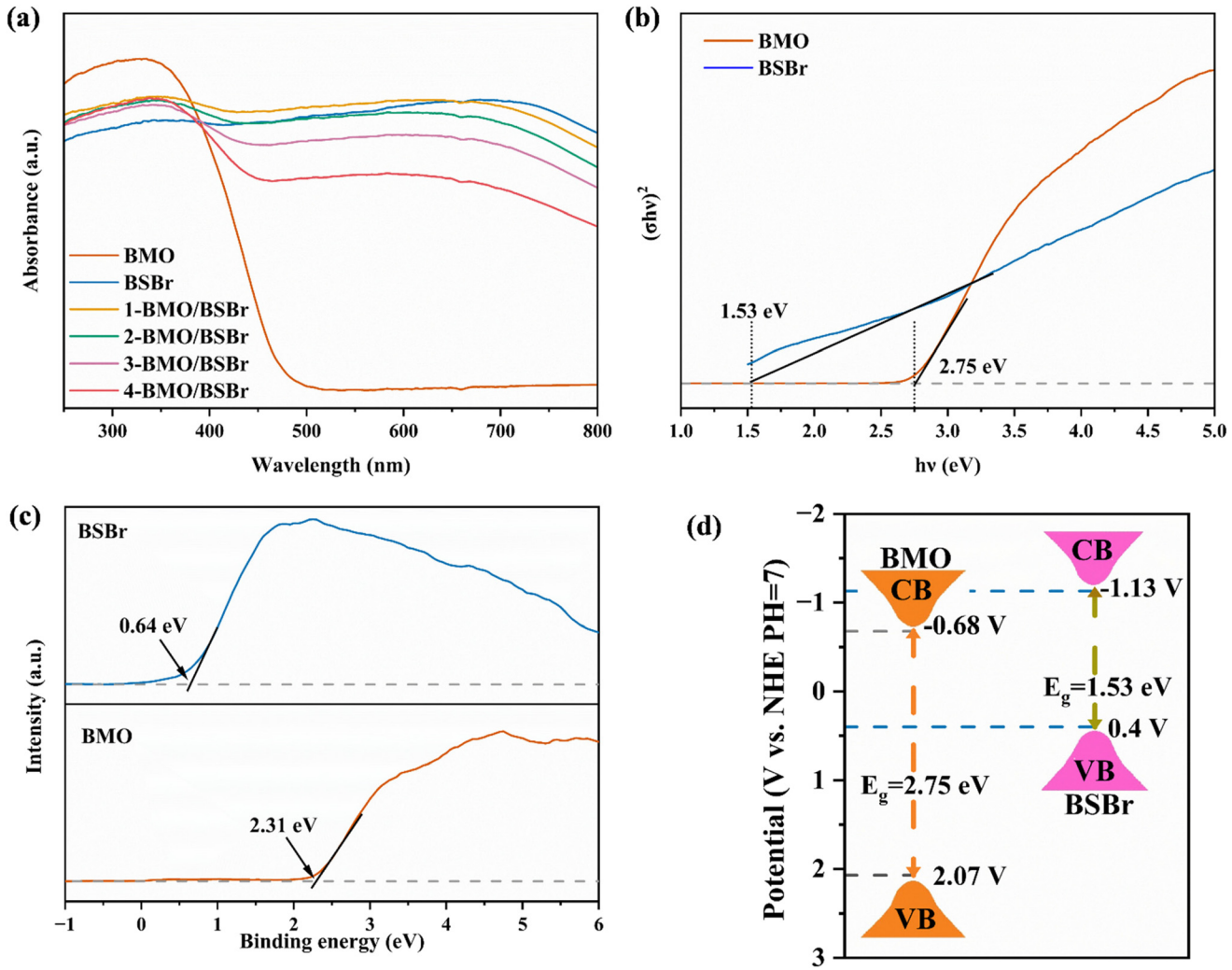

Fig. 4 (a) UV/vis DRS spectra of the prepared samples. (b) Band gaps for BMO and BSBr samples. (c) VB XPS spectra for BMO and BSBr samples. (d) The schematic energy level diagrams of BMO and BSBr samples.

morphologies of BSBr NRs that typically exhibit fewer mesopores and lower specific surface areas. The enhancement is attributed to the increased surface undulations resulting from the attachment and integration of 1D BSBr NRs.

Charge separation and transfer

The variations in the efficiency of photogenerated electron–hole separation among the synthesized samples were thoroughly evaluated using photoluminescence (PL) spectroscopy. Generally, the separation rate efficiency is inversely proportional to the PL emission intensity, where lower PL intensity typically indicates a lower recombination rate and higher efficiency.[88–90] To assess this, PL spectra were recorded at an excitation wavelength of 325 nm for the samples BMO, BSBr, and 2-BMO/BSBr (Fig. 5a). The samples BMO and 2-BMO/BSBr revealed broad emission peaks centered at around 450 nm, while the PL spectra of BSBr displayed emission peaks centered at approximately 430 nm. A closer examination showed that 2-BMO/BSBr exhibited notably lower PL emission intensity compared to the bare BMO and BSBr samples.

Additionally, the emission peak of the composite was broader, further indicating that the recombination of photo-induced charges was effectively suppressed at the interface of the two materials, thereby improving the overall photocatalytic performance.

Transient photoresponse (TPR) and electrochemical impedance spectroscopy (EIS) were used to evaluate the charge transfer and separation efficiency of the synthesized BMO, BSBr, and 2-BMO/BSBr materials. The TPR test conducted under intermittent irradiation with a 20-second interval is depicted in Fig. 4b. The photocurrent densities of BMO, BSBr, and 2-BMO/BSBr exhibited significant fluctuations, rapidly increasing and decreasing when the light illumination was turned on and off, respectively. This behavior reflects their strong photoelectric conversion ability under light irradiation. Notably, the 2-BMO/BSBr composite revealed a substantially higher photocurrent density compared to the pristine BMO

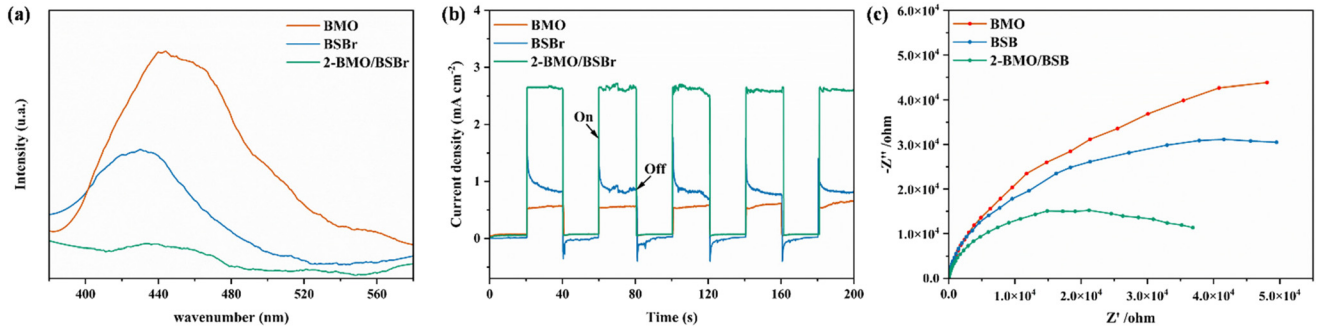

Fig. 5 (a) PL spectra, (b) TPR, and (c) EIS of BMO, BSBr, and 2-BMO/BSBr samples.

and BSBr samples, indicating enhanced separation efficiency of electron–hole pairs within the heterostructure. For pure BSBr, the initial cycles of light illumination and darkness generated a large photocurrent under illumination and a lower photocurrent in the absence of light, followed by rapid on-and-off spikes. This phenomenon is attributed to the recombination of photoinduced electron–hole pairs at the interface between the electrode and the electrolyte. In contrast, 2-BMO/BSBr exhibits a distinct behavior when the light source is turned on or off, without the spike behavior observed for BSBr.

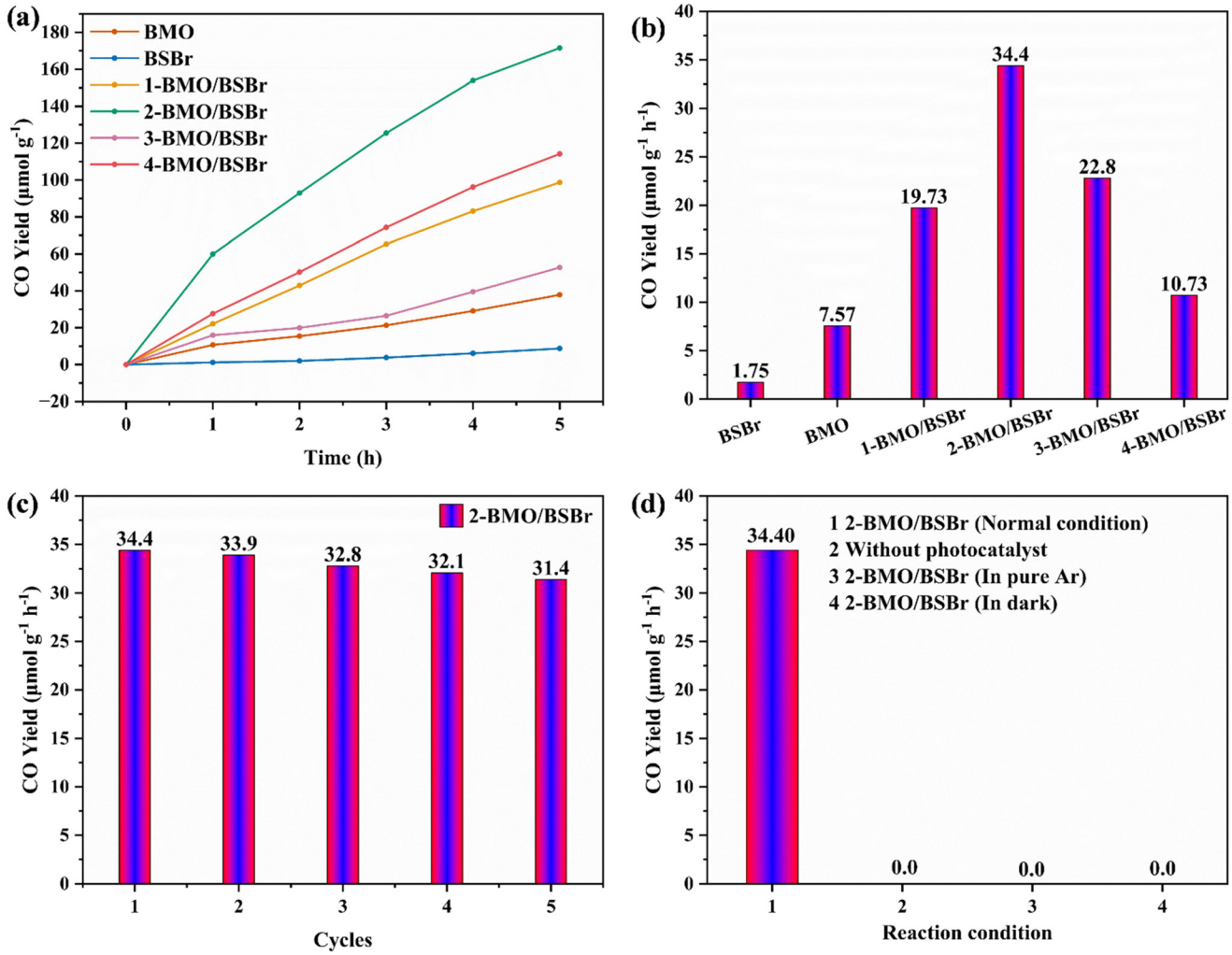

Fig. 6 (a and b) Photocatalytic CO evolution for the prepared samples. (c) Stability of the 2-BMO/BSBr sample. (d) CO evolution rates under control conditions for the 2-BMO/BSBr sample.

In addition, the photocurrent density drops smoothly to zero, unlike the changes seen in BSBr. This decay indicates that 2-BMO/BSBr effectively suppresses the recombination of charge carriers, further confirming its superior charge separation properties.[65,71] Fig. 4c shows the EIS spectra of the synthesized samples. The arc radius of 2-BMO/BSBr is markedly smaller than those of BMO and BSBr, indicating significantly reduced interfacial charge carrier transfer resistance for 2-BMO/BSBr. When considering these findings alongside the PL spectroscopy and EIS results, it can be concluded that the 2-BMO/BSBr heterostructure exhibits superior charge carrier dynamics.

Photocatalytic CO_2 reduction

The photocatalytic CO_2 reduction experiments of BMO, BSBr, and the BMO/BSBr composite are carried out in water in the absence of a sacrificial agent under visible light irradiation. As shown in Fig. 6a, the measured CO production at hourly intervals over a five-hour duration exhibits approximately linear behavior, increasing with rising irradiation exposure time for all catalysts. After 5 h of light irradiation (Fig. 6b), the CO production rates of BMO and BSBr are only 7.57 and 1.75 μmol g^{-1} h^{-1}, respectively. In contrast, BMO/BSBr catalysts exhibit substantially higher CO yields compared to BMO and BSBr. Among them, 2-BMO/BSBr shows an optimal CO production rate of 34.4 μmol g^{-1} h^{-1}, representing a 4.5-fold and 19.78-fold increase compared to BMO and BSBr, respectively. Also, Fig. S7 shows photocatalytic CO evolution for the prepared samples under full spectrum irradiation. Moreover, NMR analysis of the 2-BMO/BSBr sample (Fig. S8) confirmed the absence of any liquid phase products. Furthermore, the 2-BMO/BSBr composite demonstrated high recyclability and durable stability, as evidenced by only a slight decrease in the CO yield rate over five consecutive photocatalytic cycles (Fig. 6c). Subsequently, the catalyst was recovered and characterized after the cyclic experiments. A comparison of the XRD characterization results of the 2-BMO/BSBr sample before and after the cyclic experiments shows no significant changes (Fig. S9), confirming that the fabricated photocatalyst possesses not only excellent catalytic stability but also remarkable structural and compositional integrity. Furthermore, three control experiments are conducted under specific conditions, including a pure nitrogen atmosphere, the absence of light, and the absence of a photocatalyst. As shown in Fig. 6d, the results reveal that no CO is formed under these conditions, confirming that the carbon source of CO is exclusively derived from CO_2. Furthermore, Isotope-labeled $^{13}CO_2$ was employed as the reaction gas source to determine whether CO production originated from the decomposition of CO_2. As shown in Fig. S10, the isotopic experiment on the 2-BMO/BSBr photocatalyst after 5 h of illumination confirms that the predominant detected product was ^{13}CO (m/z = 29), unequivocally

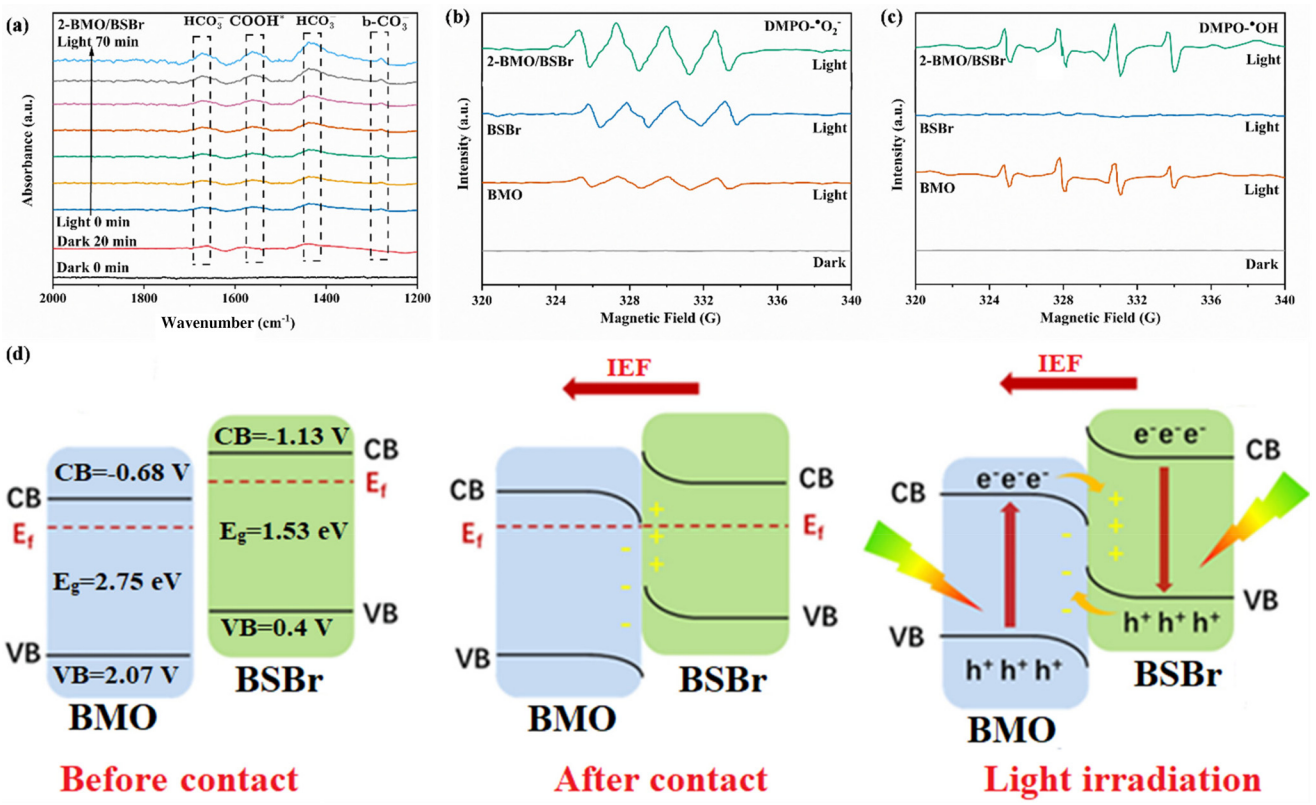

Fig. 7 (a) *In situ* DRIFTS spectra of 2-BMO/BSBr composites. EPR spectra of (b) DMPO-$^{\bullet}O_2^-$ and (c) DMPO-$^{\bullet}OH$ of BMO, BSBr, and 2-BMO/BSBr samples. (d) Band structure for 2-BMO/BSBr.

proving that the generated CO is exclusively derived from the photocatalytic CO_2 reduction.[91,92]

2D/1D heterojunction mechanism

To explore the photocatalytic CO_2 conversion mechanism over 2-BMO/BSBr, *in situ* diffuse reflectance infrared Fourier transform spectroscopy (DRIFTS) was performed. As shown in Fig. 7a, the absorption band at approximately 1275 cm^{-1} can be attributed to bidentate carbonate (b-CO_3^{-2}),[93] while the absorbance peaks at 1437 cm^{-1} and 1672 cm^{-1} correspond to bicarbonate (HCO_3^{-1}).[93,94] Additionally, the peak at 1552 cm^{-1} is indicative of the *COOH species.[95] The formation of *COOH is a critical intermediate step in photocatalytic CO_2 reduction to CO.[96] Initially, CO_2 molecules are adsorbed onto the active sites of the 2-BMO/BSBr surface. Subsequently, the reaction processes involving H^+ and e^- facilitate the transformation of CO_2 into *COOH, which is further converted to CO. Finally, CO desorbs from the catalyst surface, completing the reaction cycle.

Moreover, for exploring the redox reaction mechanism and the active species during photocatalytic CO_2 reduction, electron paramagnetic resonance (EPR) measurements were carried out under light irradiation using a 300 W Xe lamp to identify the formation of superoxide radicals ($^{\bullet}O_2^-$) and hydroxyl radicals ($^{\bullet}OH$) over BMO, BSBr, and 2-BMO/BSBr. In these measurements, 5,5-dimethyl-1-pyrroline-*N*-oxide (DMPO) was used as the spin-trapping reagent. As shown in Fig. 7b, no diffraction peaks were observed in the dark for all the studied samples. The DMPO-$^{\bullet}O_2^-$ signals (1 : 1 : 1 : 1) for BMO and BSBr can be observed because their CB potential is more negative than that of $O_2/^{\bullet}O_2^-$ (-0.33 V, pH = 7).[29,67] Fig. 7c shows the EPR spectra of DMPO-$^{\bullet}OH$ (1 : 2 : 2 : 1) for BMO, BSBr, and 2-BMO/BSBr.[76] Typically, BMO and 2-BMO/BSBr show significant DMPO-$^{\bullet}OH$ signals, while BSBr shows a negligible signal. This is because the potential of $H_2O/^{\bullet}OH$ (1.90 V, pH = 7) is more positive than the VB potential of BSBr, making it difficult for BSBr to oxidize H_2O or OH^- to $^{\bullet}OH$.[28,71]

By combining the results of DMPO-EPR radical trapping experiments with XPS evidence for the formation of strong interfacial chemical interactions and a built-in IEF, it can be concluded that the photogenerated electrons and holes are predominantly accumulated on the BSBr and BMO components of the 2-BMO/BSBr composite, respectively. This spatial charge distribution is characteristic of a direct Z-scheme heterojunction, as illustrated in Fig. 7d, rather than a conventional type-II charge transfer pathway. Upon light irradiation (Fig. 7d), electrons in both semiconductors are excited from the VB to the CB. Subsequently, the photoinduced electrons in the CB of BMO spontaneously migrate toward and recombine with the holes in the VB of BSBr, following the established Z-scheme mechanism.[33–36]

Conclusions

In summary, we have successfully fabricated a direct Z-scheme BMO/BSBr heterojunction photocatalyst incorporating a built-in IEF and interfacial bond interactions, which drastically enhance photocatalytic CO_2 reduction performance. Specifically, the formation of the direct Z-scheme heterojunction can significantly enhance the photogenerated charge carrier separation efficiency and redox capability of BMO/BSBr. Under visible-light irradiation, the optimized 2-BMO/BSBr exhibits an outstanding photocatalytic CO production rate of 34.3 μmol g^{-1} h^{-1}, outperforming pristine BMO and BSBr by 4.5 and 19.7 times, respectively. Moreover, BMO/BSBr demonstrates exceptional stability, maintaining >90% of its initial activity after cyclic tests. These findings provide a foundation for developing advanced heterojunction materials with atomic-level interfacial engineering for sustainable solar energy conversion applications.

Conflicts of interest

There are no conflict to declare.

Data availability

All data needed to evaluate the conclusions in the paper are present in the paper and the supplementary information (SI). Supplementary information is available. See DOI: https://doi.org/10.1039/d5nr05061h.

Additional data related to this paper may be requested from the authors.

Acknowledgements

This work was financially supported in part by the NSFC (52261135635 and U23A2091).

References

1 D. Lee, X. Gao, L. Sun, Y. Jee, J. Poplawsky, T. O. Farmer, L. Fan, E.-J. Guo, Q. Lu and W. T. Heller, *Nat. Commun.*, 2020, **11**, 1371.
2 J. Li, L. Cai, J. Shang, Y. Yu and L. Zhang, *Adv. Mater.*, 2016, **28**, 4059–4064.
3 H. Shang, X. Zhou, J. Dong, A. Li, X. Zhao, Q. Liu, Y. Lin, J. Pei, Z. Li and Z. Jiang, *Nat. Commun.*, 2020, **11**, 3049.
4 H. Yu, F. Chen, X. Li, H. Huang, Q. Zhang, S. Su, K. Wang, E. Mao, B. Mei and G. Mul, *Nat. Commun.*, 2021, **12**, 4594.
5 H. Yu, J. Li, Y. Zhang, S. Yang, K. Han, F. Dong, T. Ma and H. Huang, *Angew. Chem., Int. Ed.*, 2019, **58**, 3880–3884.
6 G. Zhang, Z. Hu, M. Sun, Y. Liu, L. Liu, H. Liu, C. P. Huang, J. Qu and J. Li, *Adv. Funct. Mater.*, 2015, **25**, 3726–3734.
7 K. Zhao, X. Nie, H. Wang, S. Chen, X. Quan, H. Yu, W. Choi, G. Zhang, B. Kim and J. G. Chen, *Nat. Commun.*, 2020, **11**, 2455.

8 R. Bhosale, S. Jain, C. P. Vinod, S. Kumar and S. Ogale, *ACS Appl. Mater. Interfaces*, 2019, **11**, 6174–6183.
9 F. Chen, H. Huang, L. Ye, T. Zhang, Y. Zhang, X. Han and T. Ma, *Adv. Funct. Mater.*, 2018, **28**, 1804284.
10 J. Di, X. Zhao, C. Lian, M. Ji, J. Xia, J. Xiong, W. Zhou, X. Cao, Y. She and H. Liu, *Nano Energy*, 2019, **61**, 54–59.
11 M. Gao, J. Yang, T. Sun, Z. Zhang, D. Zhang, H. Huang, H. Lin, Y. Fang and X. Wang, *Appl. Catal., B*, 2019, **243**, 734–740.
12 D. Wu, L. Ye, H. Y. Yip and P. K. Wong, *Catal. Sci. Technol.*, 2017, **7**, 265–271.
13 M. Wang, M. Shen, X. Jin, J. Tian, M. Li, Y. Zhou, L. Zhang, Y. Li and J. Shi, *ACS Catal.*, 2019, **9**, 4573–4581.
14 Y. Wang, J. Hu, T. Ge, F. Chen, Y. Lu, R. Chen, H. Zhang, B. Ye, S. Wang and Y. Zhang, *Adv. Mater.*, 2023, **35**, 2302538.
15 Z. Sun, X. Yang, X.-F. Yu, L. Xia, Y. Peng, Z. Li, Y. Zhang, J. Cheng, K. Zhang and J. Yu, *Appl. Catal., B*, 2021, **285**, 119790.
16 Y. Zhou, Y. Zhang, M. Lin, J. Long, Z. Zhang, H. Lin, J. C. S. Wu and X. Wang, *Nat. Commun.*, 2015, **6**, 8340.
17 S. Fang, M. Rahaman, J. Bharti, E. Reisner, M. Robert, G. A. Ozin and Y. H. Hu, *Nat. Rev. Methods Primers*, 2023, **3**, 61.
18 H. Zhou, D. Zhang, H. Xie, Y. Liu, C. Meng, P. Zhang, F. Fan, R. Li and C. Li, *Adv. Mater.*, 2023, **35**, 2300914.
19 J. Wu, X. Li, W. Shi, P. Ling, Y. Sun, X. Jiao, S. Gao, L. Liang, J. Xu and W. Yan, *Angew. Chem.*, 2018, **130**, 8855–8859.
20 A. Kumar and V. Krishnan, *Adv. Funct. Mater.*, 2021, **31**, 2009807.
21 F. Chen, T. Ma, T. Zhang, Y. Zhang and H. Huang, *Adv. Mater.*, 2021, **33**, 2005256.
22 X. Feng, R. Zheng, C. Gao, W. Wei, J. Peng, R. Wang, S. Yang, W. Zou, X. Wu and Y. Ji, *Nat. Commun.*, 2022, **13**, 2146.
23 Y. Shi, G. Zhan, H. Li, X. Wang, X. Liu, L. Shi, K. Wei, C. Ling, Z. Li and H. Wang, *Adv. Mater.*, 2021, **33**, 2100143.
24 J. Liang, H. Zhang, Q. Song, Z. Liu, J. Xia, B. Yan, X. Meng, Z. Jiang, X. W. Lou and C. S. Lee, *Adv. Mater.*, 2024, **36**, 2303287.
25 Z. Zhang, J. Huang, M. Zhang, Q. Yuan and B. Dong, *Appl. Catal., B*, 2015, **163**, 298–305.
26 N. Li, X. Chen, J. Wang, X. Liang, L. Ma, X. Jing, D.-L. Chen and Z. Li, *ACS Nano*, 2022, **16**, 3332–3340.
27 J. Fu, Q. Xu, J. Low, C. Jiang and J. Yu, *Appl. Catal., B*, 2019, **243**, 556–565.
28 Z. Wang, B. Cheng, L. Zhang, J. Yu and H. Tan, *Sol. RRL*, 2022, **6**, 2100587.
29 J. Wang, Y. Yu, J. Cui, X. Li, Y. Zhang, C. Wang, X. Yu and J. Ye, *Appl. Catal., B*, 2022, **301**, 120814.
30 L. Zhang, J. Zhang, J. Yu and H. García, *Nat. Rev. Chem.*, 2025, 1–15.
31 M. Sayed, K. Qi, X. Wu, L. Zhang, H. García and J. Yu, *Chem. Soc. Rev.*, 2025, **54**, 4874–4921.
32 X. Wu, M. Sayed, G. Wang, W. Yu and B. Zhu, *Adv. Mater.*, 2025, e11322.
33 F.-J. Zhang, Z.-C. Wang, Y.-H. Niu and J. Ma, *Solid State Sci.*, 2025, 108139.
34 J. Lian, D. Li, Y. Ma, H. Bian, Y. Shao, Z. Wang, J. Yan, R. Jiang, S. F. Liu and F. Zhang, *Chin. Chem. Lett.*, 2025, 111394.
35 Y.-D. Feng, Y. Zhang, D.-D. Cheng, Y.-Y. Jia, H.-R. Zhu and L. Duan, *Mol. Catal.*, 2025, **585**, 115368.
36 L. Zhang, X. Yin, X. Liu, W. Zhang, Y. Tian, X. Li, B. Li and S. Su, *J. Photochem. Photobiol., A*, 2025, **460**, 116122.
37 L. Zhang, J. Zhang, H. Yu and J. Yu, *Adv. Mater.*, 2022, **34**, 2107668.
38 F. Xu, K. Meng, B. Zhu, H. Liu, J. Xu and J. Yu, *Adv. Funct. Mater.*, 2019, **29**, 1904256.
39 Z. Liu, X. Chang, Y. Shi and X. Zhao, *J. Alloys Compd.*, 2025, **1010**, 177572.
40 Y. Huo, X. Zhou, F. Zhao, C. Ai, Z. Wu, Z. Chang and B. Zhu, *Acta Phys.-Chim. Sin.*, 2025, 100148.
41 S. Wu, M. Xu, L. Ai, Q. Ma, C. Leng, N. Guo, H. Fan and L. Wang, *J. Colloid Interface Sci.*, 2025, 138807.
42 J. Lee, G. I. Waterhouse, Y. Mao, Z. Wang, E. Zhu, J. Low, S.-P. Chai and L.-L. Tan, *Appl. Catal., B*, 2025, **365**, 124942.
43 H. Yang, Z. Wang, J. Zhang, K. Dai and J. Low, *J. Materiomics*, 2025, **11**, 100996.
44 Z. Xing, J. Hu, M. Ma, H. Lin, Y. An, Z. Liu, Y. Zhang, J. Li and S. Yang, *J. Am. Chem. Soc.*, 2019, **141**, 19715–19727.
45 J. Li, G. Zhan, Y. Yu and L. Zhang, *Nat. Commun.*, 2016, **7**, 11480.
46 Z.-K. Shen, M. Cheng, Y.-J. Yuan, L. Pei, J. Zhong, J. Guan, X. Li, Z.-J. Li, L. Bao and X. Zhang, *Appl. Catal., B*, 2021, **295**, 120274.
47 Y. Zhang, Y. Huang, S. S. Zhu, Y. Y. Liu, X. Zhang, J. J. Wang and A. Braun, *Small*, 2021, **17**, 2100320.
48 Y. Ao, J. Xu, P. Wang, C. Wang, J. Hou, J. Qian and Y. Li, *Colloids Surf., A*, 2015, **487**, 66–74.
49 S. Salehian, A. Larimi, A. A. Asgharinezhad, N. Khallaghi, T. N. Borhani and C. Ghotbi, *Surf. Interfaces*, 2023, **42**, 103432.
50 Z. Liu, Y. Song, Q. Wang, Y. Jia, X. Tan, X. Du and S. Gao, *J. Colloid Interface Sci.*, 2019, **556**, 92–101.
51 J. Chi, Z. Jiang, J. Yan, A. Larimi, Z. Wang, L. Wang and W. Shangguan, *Mater. Today Chem.*, 2022, **26**, 101060.
52 M. Mehta, S. Krishnamurthy, S. Basu, T. P. Nixon and A. P. Singh, *Mater. Today Chem.*, 2020, **17**, 100283.
53 H. S. M. Abd-Rabboh, M. Benaissa, M. S. Hamdy, M. A. Ahmed and M. Glal, *Opt. Mater.*, 2021, **114**, 110761.
54 H. Li, L. Liang, X. Niu, D. Zhang, H. Fan and K. Wang, *New J. Chem.*, 2022, **46**, 8185–8194.
55 X. Song, R. Wang, J. Wang, Z. Huang, S. Ye and D. D. Dionysiou, *Opt. Mater.*, 2021, **113**, 110839.
56 M. Ahmadi, S. M. Alavi and A. Larimi, *Catal. Commun.*, 2023, **179**, 106681.
57 Q. Wang, K. Wang, L. Zhang, H. Wang and W. Wang, *Appl. Surf. Sci.*, 2019, **470**, 832–839.

58 L. Cheng, L. Liu, D. Wang, F. Yang and J. Ye, *J. CO2 Util.*, 2019, **29**, 196–204.
59 L. Liu, K. Dai, J. Zhang and L. Li, *J. Colloid Interface Sci.*, 2021, **604**, 844–855.
60 Y. Dong, S. Dong, B. Liu, C. Yu, J. Liu, D. Yang, P. Yang and J. Lin, *Adv. Mater.*, 2021, **33**, 2106838.
61 L. Zhang, T. Xu, X. Zhao and Y. Zhu, *Appl. Catal., B*, 2010, **98**, 138–146.
62 N. Li, L. Zhu, W.-D. Zhang, Y.-X. Yu, W.-H. Zhang and M.-F. Hou, *J. Alloys Compd.*, 2011, **509**, 9770–9775.
63 X. Zhang, G. Ren, C. Zhang, R. Li, Q. Zhao and C. Fan, *Catal. Lett.*, 2020, **150**, 2510–2516.
64 F. Deng, F. Zhong, L. Zhao, X. Luo, S. Luo and D. D. Dionysiou, *J. Hazard. Mater.*, 2017, **340**, 85–95.
65 L. Ai, L. Wang, M. Xu, S. Zhang, N. Guo, D. Jia and L. Jia, *Appl. Catal., B*, 2021, **284**, 119730.
66 Y. Chen, G. Tian, T. Feng, W. Zhou, Z. Ren, T. Han, Y. Xiao and H. Fu, *CrystEngComm*, 2015, **17**, 6120–6126.
67 J. Zhao, M. Ji, H. Chen, Y.-X. Weng, J. Zhong, Y. Li, S. Wang, Z. Chen, J. Xia and H. Li, *Appl. Catal., B*, 2022, **307**, 121162.
68 J. Li, W. Pan, Q. Liu, Z. Chen, Z. Chen, X. Feng and H. Chen, *J. Am. Chem. Soc.*, 2021, **143**, 6551–6559.
69 W. Jia, R. Xiong, Y. Sun, Y. Xiao, B. Cheng and S. Lei, *J. Mater. Chem. A*, 2024, **12**, 4513–4524.
70 R. Niu, Q. Liu, B. Huang, Z. Liu, W. Zhang, Z. Peng, Z. Wang, Y. Yang, Z. Gu and J. Li, *Appl. Catal., B*, 2022, **317**, 121727.
71 X. Li, J. Zhang, Z. Wang, J. Fu, S. Li, K. Dai and M. Liu, *Chem. – Eur. J.*, 2023, **29**, e202202669.
72 X. Wu, Q. Zhang and C. Su, *FlatChem*, 2021, **27**, 100244.
73 Z. Zhang, T. Zheng, J. Xu and H. Zeng, *J. Mater. Sci.*, 2016, **51**, 3846–3853.
74 A. Phuruangrat, P. Jitrou, P. Dumrongrojthanath, N. Ekthammathat, B. Kuntalue, S. Thongtem and T. Thongtem, *J. Nanomater.*, 2013, **2013**(1), 789705.
75 J. He, J. Lin, Y. Zhang, Y. Hu, Q. Huang, G. Zhou, W. Li, J. Hu, N. Hu and Z. Yang, *Chem. Eng. J.*, 2024, **480**, 148036.
76 J. Zhang, M. Zheng, Y. Wu, J. Xiong, S. Li, W. Jiang, Z. Liu and J. Di, *ACS Nano*, 2025, **19**, 2759–2768.
77 X. Xie, Q.-U. Hassan, H. Lu, F. Rao, J. Gao and G. Zhu, *Chin. Chem. Lett.*, 2021, **32**, 2038–2042.
78 X. Li, W. Zhang, J. Li, G. Jiang, Y. Zhou, S. Lee and F. Dong, *Appl. Catal., B*, 2019, **241**, 187–195.
79 W. C. Huo, J. Y. Li, M. Liu, X. Y. Liu, Y. X. Zhang and F. Dong, *Chem. Eng. J.*, 2019, **361**, 129–138.
80 E. A. Abdullah, A. H. Abdullah, Z. Zainal, M. Z. Hussein and T. K. Ban, *J. Chem.*, 2012, **9**, 2429–2438.
81 S. M. Ramay, H. Kassim, A. Mahmood, A. A. Siddig and N. S. Al Zayed, *J. Mater. Sci.: Mater. Electron.*, 2022, **33**, 14343–14355.
82 R. K. Chava, Y. Im and M. Kang, *J. Mater. Chem. A*, 2024, **12**, 18498–18511.
83 M. Jin, S. Lu, L. Ma and M. Gan, *Appl. Surf. Sci.*, 2017, **396**, 438–443.
84 Z. Cai, Y. Huang, H. Ji, W. Liu, J. Fu and X. Sun, *Sep. Purif. Technol.*, 2022, **280**, 119772.
85 C. Li, S. Gu, Y. Xiao, X. Lin, X. Lin, X. Zhao, J. Nan and X. Xiao, *J. Colloid Interface Sci.*, 2024, **668**, 426–436.
86 S. Maswanganyi, R. Gusain, N. Kumar, E. Fosso-Kankeu, F. B. Waanders and S. S. Ray, *ACS Omega*, 2021, **6**, 16783–16794.
87 J. Zhao, Q. Lu, M. Wei and C. Wang, *J. Alloys Compd.*, 2015, **646**, 417–424.
88 B. Huang, X. Fu, K. Wang, L. Wang, H. Zhang, Z. Liu, B. Liu and J. Li, *Adv. Powder Mater.*, 2024, **3**, 100140.
89 R. Yuan, C. Yue, J. Qiu, F. Liu and A. Li, *Appl. Catal., B*, 2019, **251**, 229–239.
90 X. Gao, G. Tang, W. Peng, Q. Guo and Y. Luo, *Chem. Eng. J.*, 2019, **360**, 1320–1329.
91 S. Wang, X. Hai, X. Ding, S. Jin, Y. Xiang, P. Wang, B. Jiang, F. Ichihara, M. Oshikiri and X. Meng, *Nat. Commun.*, 2020, **11**, 1149.
92 Z. K. Xin, Y. J. Gao, Y. Gao, H. W. Song, J. Zhao, F. Fan, A. D. Xia, X. B. Li, C. H. Tung and L. Z. Wu, *Adv. Mater.*, 2022, **34**, 2106662.
93 B. Wang, J. Di, L. Lu, S. Yan, G. Liu, Y. Ye, H. Li, W. Zhu, H. Li and J. Xia, *Appl. Catal., B*, 2019, **254**, 551–559.
94 X. Li, L. Liang, Y. Sun, J. Xu, X. Jiao, X. Xu, H. Ju, Y. Pan, J. Zhu and Y. Xie, *J. Am. Chem. Soc.*, 2018, **141**, 423–430.
95 X. Li, Y. Sun, J. Xu, Y. Shao, J. Wu, X. Xu, Y. Pan, H. Ju, J. Zhu and Y. Xie, *Nat. Energy*, 2019, **4**, 690–699.
96 J. Di, C. Chen, S.-Z. Yang, S. Chen, M. Duan, J. Xiong, C. Zhu, R. Long, W. Hao and Z. Chi, *Nat. Commun.*, 2019, **10**, 2840.